

Disparate effects of circumgalactic medium angular momentum in IllustrisTNG and SIMBA

Kexin Liu^{1,2,*}, Hong Guo^{1,*}, Sen Wang³, Dandan Xu³, Shengdong Lu⁴,
Weiguang Cui^{5,6,7}, and Romeel Davé^{7,8,9}

¹ Shanghai Astronomical Observatory, Chinese Academy of Sciences, Shanghai 200030, China

² University of Chinese Academy of Sciences, Beijing 100049, China

³ Department of Astronomy, Tsinghua University, Beijing 100084, China

⁴ Institute for Computational Cosmology, Department of Physics, University of Durham, South Road, Durham DH1 3LE, UK

⁵ Departamento de Física Teórica, M-8, Universidad Autónoma de Madrid, Cantoblanco E-28049, Madrid, Spain

⁶ Centro de Investigación Avanzada en Física Fundamental (CIAFF), Universidad Autónoma de Madrid, Cantoblanco E-28049, Madrid, Spain

⁷ Institute for Astronomy, University of Edinburgh, Royal Observatory, Edinburgh EH9 3HJ, UK

⁸ University of the Western Cape, Bellville, Cape Town 7535, South Africa

⁹ South African Astronomical Observatories, Observatory, Cape Town 7925, South Africa

Received 14 September 2024 / Accepted 20 November 2024

ABSTRACT

In this study, we examine the role of the circumgalactic medium (CGM) angular momentum (j_{CGM}) on star formation in galaxies, whose influence is currently not well understood. The analysis utilises central galaxies from two hydrodynamical simulations, SIMBA and IllustrisTNG. We observe a substantial divergence in how star formation rates correlate with CGM angular momentum between the two simulations. Specifically, quenched galaxies in IllustrisTNG show higher j_{CGM} than their star-forming counterparts with similar stellar masses, while the reverse is true in SIMBA. This difference is attributed to the distinct active galactic nucleus (AGN) feedback mechanisms active in each simulation. Moreover, both simulations demonstrate similar correlations between j_{CGM} and environmental angular momentum (j_{Env}) in star-forming galaxies, but these correlations change notably when kinetic AGN feedback is present. In IllustrisTNG, quenched galaxies consistently show higher j_{CGM} compared to their star-forming counterparts with the same j_{Env} , a trend not seen in SIMBA. Examining different AGN feedback models in SIMBA, we further confirm that AGN feedback significantly influences the CGM gas distribution, although the relationship between the cold gas fraction and the star formation rate (SFR) remains largely stable across different feedback scenarios.

Key words. galaxies: evolution – galaxies: formation – galaxies: kinematics and dynamics

1. Introduction

The structure and star formation activity of a galaxy are closely linked to its kinematic properties. It has been proposed that disc galaxies are formed from gas accretion and acquire angular momentum from tidal torques (see e.g., Fall & Efstathiou 1980; Barnes & Efstathiou 1987; Mo et al. 1998; Bullock et al. 2001; Kereš et al. 2005). On the other hand, elliptical galaxies have a factor of five less angular momentum than disc galaxies of similar masses (e.g., Fall 1983; Romanowsky & Fall 2012; Fall & Romanowsky 2013).

Thanks to large-scale integral field spectroscopy (IFS) surveys, galaxies can be further classified by their dynamical features rather than by simple morphology or colour (Driver et al. 2007). The SAURON project (Bacon et al. 2001), which is based on the IFS, complements the traditional classification of early-type galaxies (ETGs) by including information about galaxy kinematics. The ETGs are divided into fast and slow rotators in the anisotropy diagram between the ratio of ordered and random motion (V/σ) and ellipticity (ε) (see e.g., Cappellari et al. 2007; Emsellem et al. 2007). van de Sande et al. (2018) further found

a strong correlation between the stellar population age and the location in the (V/σ , ε) diagram, where fast rotators are younger and slow rotators are relatively old. This suggests that the star formation history is correlated with galaxy stellar kinematics.

The circumgalactic medium (CGM) is believed to be a source of fuel for star formation and is thus expected to be linked to star formation activity. Using the IllustrisTNG hydrodynamical simulation (hereafter TNG; Pillepich et al. 2018; Nelson et al. 2019b), Lu et al. (2022) found that quenched early-type galaxies typically have higher specific angular momenta than their star-forming disc counterparts with similar stellar masses. This high angular momentum of the CGM could impede the efficient radial gas inflow that is necessary to maintain star formation in the centre and is thus seen as an additional factor in keeping galaxies quenched, a process known as angular momentum quenching (Peng & Renzini 2020). The high angular momenta of quenched galaxies in TNG are probably related to the more frequent prograde merger events (relative to the spin of the galaxy itself, as the angular momentum of the CGM gas is inherited from the large-scale halo environment (Lu et al. 2022; Wang et al. 2022b).

However, the angular momentum and gas distributions of galaxies in hydrodynamical simulations can be easily altered by the baryon physics employed. Negative feedback from the

* Corresponding authors; liukexin@shao.ac.cn,
guohong@shao.ac.cn

active galactic nucleus (AGN) is one of the most effective ways to quench galaxies in these simulations. Ma et al. (2022) compared the hydrodynamical simulations of TNG and SIMBA (Davé et al. 2019) and found that the kinetic AGN feedback in TNG only moves cold gas from the inner discs to the outer regions, thus reducing the star formation activities in the inner regions. This leads to TNG overestimating the overall cold-gas reservoir in quenched galaxies compared to observations. Therefore, angular momentum quenching is necessary in TNG to prevent the CGM gas of these quenched galaxies from falling into the centre. On the other hand, the bipolar injection of kinetic AGN feedback in SIMBA only slightly reduces the cold gas densities in the inner regions, but significantly heats the CGM gas, which brings SIMBA into better agreement with the observed cold-gas masses for quenched galaxies. Without a consistent supply of cold gas in the CGM, quenched galaxies will remain with low star formation rates, so it does not seem necessary to have the additional input of angular momentum quenching.

It is perplexing to consider the impact of angular momentum on star formation in galaxies when comparing the two simulations. To gain a better understanding of the effect of angular momentum in different hydrodynamical simulations, this paper will explore the relationship between star formation rate (SFR) and CGM angular momentum in TNG and SIMBA. In addition, we will examine the influence of various morphologies on the angular momentum distribution. The paper is organised as follows. Section 2 provides an overview of the galaxy samples in the two simulations. The main findings are summarised in Section 3. Conclusions and discussions are described in Section 4.

2. Simulation and data

2.1. The IllustrisTNG simulation

The IllustrisTNG project consists of a set of magnetohydrodynamical simulations of different cosmological volumes (Marinacci et al. 2018; Naiman et al. 2018; Nelson et al. 2018, 2019b; Pillepich et al. 2018; Springel et al. 2018), run with the Arepo code (Springel 2010). In this paper, we focus on the TNG100-1 simulation with a box size of $75 h^{-1}$ Mpc on a side, and the cosmological parameters are $\Omega_m = 0.3089$, $\Omega_\lambda = 0.6911$, $\Omega_b = 0.0486$, and $h = 0.6774$. The dark matter mass resolution is $m_{\text{DM}} = 7.5 \times 10^6 M_\odot$ and the average gas cell mass is around $m_{\text{gas}} = 1.4 \times 10^6 M_\odot$.

The Illustris simulation (Vogelsberger et al. 2014) has been improved by the TNG model with the introduction of two AGN feedback modes: thermal and kinetic. These two modes are exclusive and are determined by comparing the Eddington ratio, λ_{Edd} , with the critical value, χ , which is calculated using equation $\chi = \min[0.002(M_{\text{BH}}/10^8 M_\odot)^2, 0.1]$. When the Eddington ratio is greater than or equal to the critical value, the thermal mode is activated, which injects energy isotropically into the environment and heats the surrounding gas. On the other hand, when the Eddington ratio is less than the critical value, the AGN feedback switches to the kinetic mode, which produces black hole-driven winds and transfers energy to the neighbouring gas in the form of random momentum (Weinberger et al. 2017). This kinetic mode has enabled the stellar mass fraction in massive haloes to be more in line with observations, without the overheating of gas as in Illustris.

2.2. The SIMBA simulation

SIMBA simulations (Davé et al. 2019) are carried out using the GIZMO code (Hopkins 2015), which is a solver for cosmological gravity and hydrodynamics. This paper adopts the flagship run of SIMBA (m100n1024), which has a box size of $100 h^{-1}$ Mpc on a side and cosmological parameters that are consistent with TNG, including $\Omega_m = 0.3$, $\Omega_\lambda = 0.7$, $\Omega_b = 0.048$, and $h = 0.68$. The resulting dark matter and gas cell mass resolutions are $9.6 \times 10^7 M_\odot$ and $1.82 \times 10^7 M_\odot$, respectively. Galaxies in SIMBA are identified by a 6D friends-of-friends (FOF) finder with a linking length of 0.0056 times the mean inter-particle distance, while haloes are identified using a 3D FoF finder with a linking length parameter of 0.2.

SIMBA assumes the H_2 -based star formation law (Schmidt 1959), where the H_2 fraction is determined by local metallicity and gas column density (Krumholz & Gnedin 2011). The star formation rate (SFR) is then calculated using the equation: $\text{SFR} = \varepsilon_* \rho_{\text{H}_2} / t_{\text{dyn}}$, where $\varepsilon_* = 0.02$ (Kennicutt 1998) and the dynamical time $t_{\text{dyn}} = 1/\sqrt{G\rho}$. The HI gas fraction is calculated based on the prescription of Rahmati et al. (2013). The total neutral gas can then be calculated on the fly. Each gas cell in haloes is assigned to the galaxy with the highest value of M_{baryon}/R^2 , where M_{baryon} is the total baryonic mass of the galaxy and R is the distance from the gas cell to the centre of the galaxy. SIMBA incorporates the star formation-driven feedback from MUFASA and a torque-limited accretion model (Hopkins & Quataert 2011; Anglés-Alcázar et al. 2017) to accrete cold gas ($T < 10^5$ K), which does not require self-regulation for black hole growth (Anglés-Alcázar et al. 2015). For hot gas ($T > 10^5$ K), Bondi accretion is used (Bondi 1952), which is the same as in TNG.

In SIMBA, two main kinetic feedback models are present, along with an X-ray feedback model. When the Eddington ratio is high ($\lambda_{\text{Edd}} > 0.2$), a radiative or wind mode is activated, which propels the gas away from the black hole at speeds of up to 1000 km s^{-1} . When the Eddington ratio is low ($\lambda_{\text{Edd}} < 0.2$) and the black hole mass is greater than $10^{7.5} M_\odot$, a jet mode is triggered, which can reach velocities of up to 8000 km s^{-1} when $\lambda_{\text{Edd}} < 0.02$. Both the jet and wind modes are bipolar and purely kinetic, and a small fraction of the energy of the jet mode will increase the virial temperature of the halo. When the full jet condition ($\lambda_{\text{Edd}} < 0.02$) and $f_{\text{H}_2} < 0.2$ is met, the X-ray heating mode is activated. This mode has the least effect on galaxies (Davé et al. 2019), and is usually insignificant.

The SIMBA project has a set of simulations with a box size of $50 h^{-1}$ Mpc on a side (simulation name m50n512), containing 2×512^3 particles (i.e. the same resolution and input physics as the flagship run m100n1024), but with a volume eight times smaller. In addition to the full m50n512 run, there are catalogues that have different AGN feedback mechanisms turned off: ‘No-Xray’, ‘No-jet’, and ‘No-AGN’, which correspond to X-ray feedback off, both X-ray and jet models off, and all AGN feedback models off, respectively. We use both m100n1024 and m50n512 runs to investigate the effect of CGM angular momentum with different feedback conditions.

2.3. Sample selection

In this paper, we focus exclusively on the central galaxies in both TNG and SIMBA. The SFR in TNG is determined from the value of ‘SubhaloSFR’, that is, the total SFR of all gas cells in a given subhalo. In SIMBA, the SFR is defined as the total SFR in gas particles belonging to each galaxy. Figure 1 displays

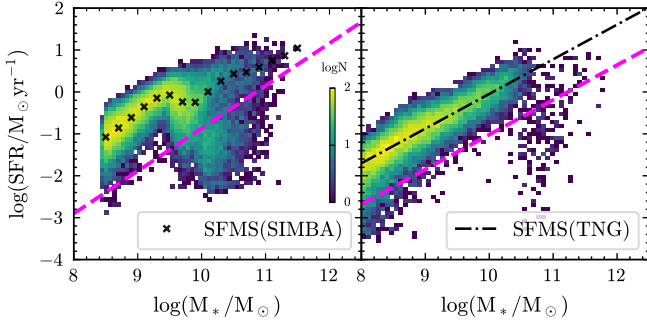


Fig. 1. Distribution of central galaxies at $z = 0$ as a function of SFR and M_* , for SIMBA and TNG in 100 Mpc/h, from left to right, respectively. The coloured background is the logarithmic number of central galaxies. The black dot-dashed line is the SFMS of TNG100, following the definition in Ma et al. (2022): $\log(\text{SFR}/\text{yr}^{-1} M_\odot) = 0.83 \log M_* - 8.32$, and black cross represents SFMS of star-forming central galaxies in SIMBA100, where star-forming galaxies are simply selected with $\log(\text{sSFR}/\text{Gyr}^{-1} M_\odot) \geq -1.8$. Magenta lines separate the star-forming and quenched galaxies in both panels.

the central galaxy distributions in the SFR– M_* plane, with the colour indicating the number density of central galaxies. We use the definitions of the star formation main sequence (SFMS) $\text{SFR}_{\text{MS}}(M_*)$ in SIMBA (left panel) and TNG (right panel) from Ma et al. (2022), which are shown as the crosses and the dot-dashed line, respectively. Since the SFMS of SIMBA is curved for $M_* > 10^{9.5} M_\odot$, we only consider galaxies with stellar masses ranging from $10^{9.5} M_\odot$ to $10^{11.2} M_\odot$ in both simulations at $z = 0$ to ensure that the galaxies in our sample are fully resolved.

Finally, we select a total of 6925 and 14479 central galaxies in the mass range of $9.5 \leq \log(M_*/M_\odot) \leq 11.2$ from SIMBA and TNG, respectively. For a fair comparison between the two simulations, we focus on the SFR offsets from the SFMS, $\Delta \log \text{SFR}$, defined as,

$$\Delta \log \text{SFR} = \log \text{SFR} - \log \text{SFR}_{\text{MS}}. \quad (1)$$

Following Ma et al. (2022), we separate the star-forming and quenched galaxies with the cutoff SFR of $\Delta \log \text{SFR} = -1$, that is, 1 dex below the SFMS.

2.4. Kinematic properties

According to Lu et al. (2022), we consider the region beyond twice the half stellar mass radius of the galaxy ($2R_{\text{hsm}}$) and within 100 kpc to be the CGM domain. Beyond this scale, the connection between CGM cold gas and inner star formation is weak. We focus on the cold phase of the CGM gas, which has a temperature range of $10^4 \text{ K} < T < 2 \times 10^4 \text{ K}$. In Wang et al. (2022b), it was found that the cold-phase CGM gas has a higher angular momentum and more tangential motion than its hot-phase ($T > 10^5 \text{ K}$) counterparts.

In both TNG and SIMBA simulations, we calculate the specific angular momentum of the cold-phase CGM gas ($10^4 \text{ K} < T < 2 \times 10^4 \text{ K}$), \mathbf{j}_{CGM} , as follows,

$$\mathbf{j}_{\text{CGM}} = \frac{\sum_i m_{\text{gas},i} \mathbf{r}_{\text{gas},i} \times \mathbf{v}_{\text{gas},i}}{\sum_i m_{\text{gas},i}}, \quad (2)$$

where $m_{\text{gas},i}$ is the mass of a given gas cell i , $\mathbf{r}_{\text{gas},i}$ is the relative distance from the galaxy centre, and $\mathbf{v}_{\text{gas},i}$ is the velocity. The summation is performed in all cold gas cells with $2R_{\text{hsm}} <$

$r_{\text{gas},i} < 100 \text{ kpc}$. The dimensionless spin of CGM (λ_{CGM}) can be measured as follows (Lu et al. 2022),

$$\lambda_{\text{CGM}} = \frac{\sum_i m_{\text{gas},i} v_{t,\text{gas},i}^2 r_{\text{gas},i} / GM(\leq r_{\text{gas},i})}{\sum_i m_{\text{gas},i}} \quad (3)$$

where $v_{t,\text{gas},i}$ is the tangential velocity of the i -th gas cell and $M(\leq r_{\text{gas},i})$ is the total mass (including all types of particles) within $r_{\text{gas},i}$.

Different from Lu et al. (2022), we calculate the environmental angular momentum of each central galaxy, \mathbf{j}_{env} , by summing the contribution from all particles (including dark matter, star, and gas particles) as,

$$\mathbf{j}_{\text{env}} = \frac{\sum_i M_{\text{par},i} \mathbf{r}_i \times \mathbf{v}_i}{\sum_i M_{\text{par},i}}, \quad (4)$$

where $M_{\text{par},i}$ is the mass of an individual particle i , \mathbf{r}_i is the relative distance from i to the central galaxy, and \mathbf{v}_i is the relative velocity. The summation is performed on all particles with $2R_{\text{hsm}} < r_i < 100 \text{ kpc}$, where dark matter will dominate the contribution of angular momentum. This will ensure a better quantification of the environmental angular momentum than just using the satellite galaxies as in Lu et al. (2022).

3. Results

3.1. Trend with SFR

In Figure 2, we show the distribution of galaxies in the $\lambda_{\text{CGM}} - \Delta \log \text{SFR}$ plane for SIMBA (top panel) and TNG (bottom panel). The colour coding indicates the logarithmic number of galaxies. The solid line in each panel indicates the median values with errors estimated from the 16th–84th percentile ranges. The two simulations show different correlations between λ_{CGM} and $\Delta \log \text{SFR}$. In TNG, galaxies with a low $\Delta \log \text{SFR}$ have much higher λ_{CGM} than their star-forming counterparts. This is in agreement with the findings of Lu et al. (2022), which suggest that the CGM gas of the quenched galaxies still has a strong rotational motion. It is likely related to the surplus of cold gas in the CGM caused by the relatively weak kinetic AGN feedback in the TNG (Ma et al. 2022).

On the other hand, λ_{CGM} gradually increases with $\Delta \log \text{SFR}$ in SIMBA and most quenched galaxies only have a small λ_{CGM} (< 0.2), indicating that the CGM gas in quenched galaxies is more likely to have random motion rather than rotational motion. This is also in line with their low cold gas reservoir, as reported in Appleby et al. (2021) and Ma et al. (2022). The majority of galaxies with high- λ_{CGM} are the disc galaxies in the SFMS.

We note that the comparisons in Figure 2 do not include galaxies without SFR measurements (i.e. $\text{SFR} = 0$) in both simulations. The fraction of galaxies with $\text{SFR} = 0$ is 3.5% and 9% for SIMBA and TNG, respectively. These galaxies are caused by the stochastic star formation algorithms and the limited simulation resolution. So they can be effectively considered as fully quenched. To be comprehensive, Figure 3 displays the probability distributions of λ_{CGM} for all quenched galaxies (including galaxies with $\text{SFR} = 0$) and star-forming galaxies in SIMBA (orange) and TNG (blue). Both the star-forming and quenched galaxies show very different distributions in λ_{CGM} between SIMBA and TNG. Star-forming galaxies in SIMBA have significantly lower λ_{CGM} compared to TNG. It is evident that the λ_{CGM} distributions for all quenched galaxies still follow the trend for quenched galaxies shown in Figure 2, whether in TNG or SIMBA. Although galaxies with $\text{SFR} = 0$ in TNG have

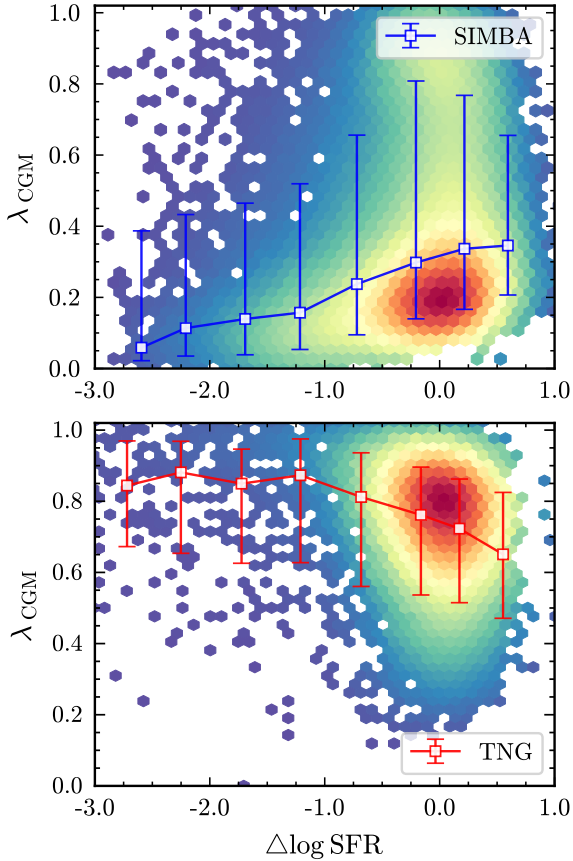


Fig. 2. Distribution of λ_{CGM} as a function of $\Delta \log \text{SFR}$ in SIMBA (top panel) and TNG (bottom panel). The background is the logarithmic number of galaxies, with colours ranging from light (blue) to dark (red) indicating an increasing number of galaxies. From top to bottom panels, the blue and red lines show the median values and errors estimated from the 16th–84th percentile ranges for SIMBA and TNG, respectively.

slightly lower λ_{CGM} values (with an average of around 0.72) than the median values (~ 0.8) shown in Figure 2, they are still comparable to the λ_{CGM} values of star-forming galaxies (with an average of 0.76), as illustrated in Figure 3. The situation is similar in SIMBA. Those with $\text{SFR} = 0$ in SIMBA have an average λ_{CGM} of 0.11, while those star-forming galaxies have an average value of 0.28.

Figure 4 presents examples of cold gas distributions in star-forming and quenched galaxies in TNG (two left panels) and SIMBA (two right panels). The top and bottom panels display face-on and edge-on projections, respectively. The colour scales indicate the SFRs of the gas cells, as labelled. The total specific SFR of each galaxy ($\text{sSFR} = \text{SFR}/M_*$) is also shown in the panel. Notably, both the star-forming and quenched galaxies in TNG have large cold-gas discs in the CGM, which is in agreement with their high angular momenta, as seen in Figure 2. However, the quenched galaxies have an obvious cavity of cold gas in the central region (roughly the size of the stellar disc). As demonstrated in Ma et al. (2022), galaxies in TNG are quenched by the ejection of cold gas from inner discs to the outer regions, which is caused by the kinetic AGN feedback mode. This naturally creates a hole in the gas distribution and halts star formation in the central stellar disc.

In contrast to star-forming galaxies, quenched galaxies in SIMBA have very few cold gas cells, and their distribution is more spherical than disc-like. Additionally, there is no visible

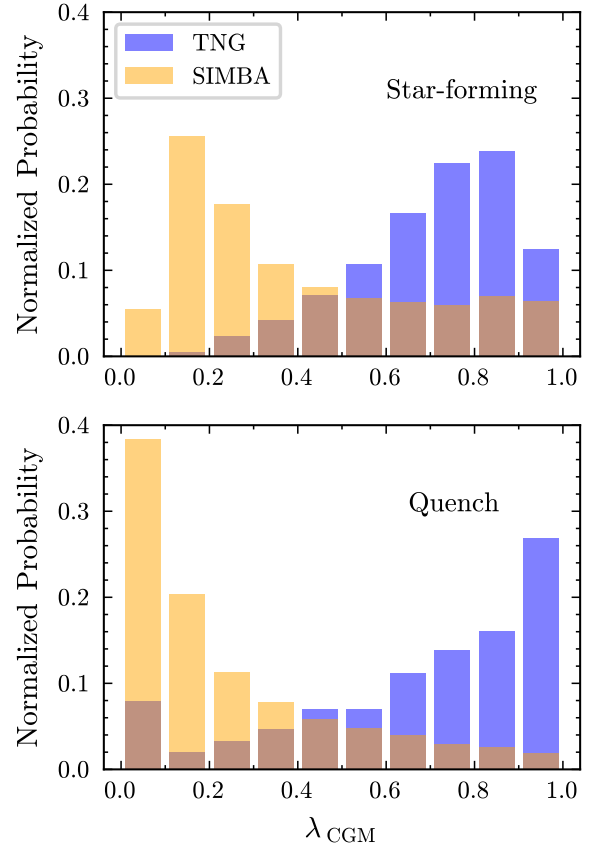


Fig. 3. Histograms of λ_{CGM} for SIMBA and TNG, with the top and bottom panels representing star-forming and quenched galaxies, respectively, where quenched galaxies include those with $\text{SFR} = 0$, and the Y-axis is normalised by the total number of central galaxies in each simulation. Blue and orange bins represent normalised probability of TNG and SIMBA, respectively, and the brown is cross area.

cavity of cold gas in the core. The cold gas density in the central parts of star-forming and quenched galaxies in SIMBA are quite similar (see Fig. 5 of Ma et al. 2022). However, the quenched galaxies have much less cold gas in the CGM, which reduces the amount of cold gas that can reach the core, and, as a result, the overall SFR decreases.

It is evident from the comparisons that galaxies in TNG and SIMBA, despite having similar stellar masses and star formation rates, have distinct CGM gas kinematics that are linked to the total cold gas supply and their AGN feedback processes.

3.2. Cold gas reservoir

To be clear, we compute the cold gas mass in the CGM, M_{gas} , by summing the cold gas cells within the range of $2R_{\text{hsm}}$ to 100 kpc. Additionally, we define $f_{\text{cold}} \equiv M_{\text{gas}}/M_*$ as the ratio of M_{gas} to the total stellar mass of galaxies (M_*). The relationship between f_{cold} and $\Delta \log \text{SFR}$ is analysed in Figure 5, with SIMBA displayed in the two left panels and TNG in the two right panels. The colour scales, as indicated by the colour bar on the right, represent the normalised galaxy number density in each simulation. We categorise the galaxy distributions into subsamples of $\lambda_{\text{CGM}} < 0.5$ and $\lambda_{\text{CGM}} > 0.5$, as labelled in each panel. It is apparent that in SIMBA, angular momentum scarcely affects the correlation between SFR and the CGM gas mass. In most quenched galaxies, the CGM shows low f_{cold} and low angular

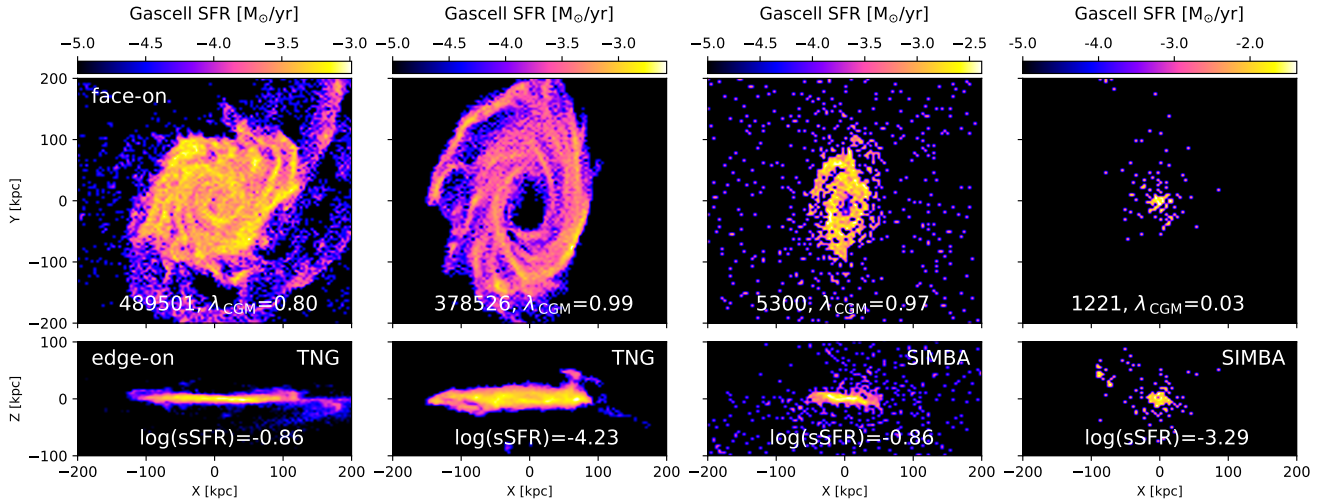


Fig. 4. Spatial distribution of cold gas in four examples of TNG and SIMBA, respectively. Stellar masses of all four galaxies are in the range of $10^{10.2} - 10^{10.8} M_{\odot}$. Top panels are shown in face-on projection, along with the direction of galaxy gas angular momentum, and bottom is in edge-on projection. The gas distribution is colour-coded by its star-formation rate, and λ_{CGM} and $\log \text{sSFR}$ (M_{\odot}/Gyr) are labelled in each panel.

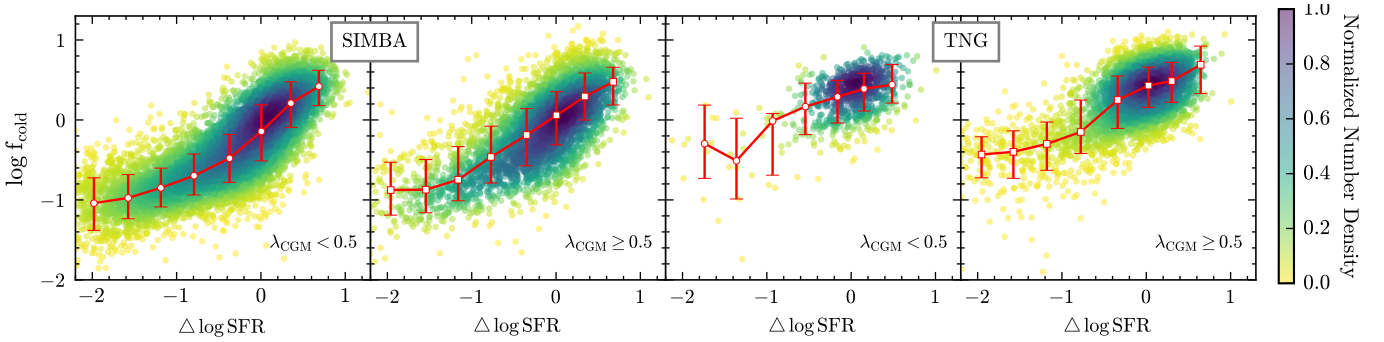


Fig. 5. Relations between $\log f_{\text{cold}}$ and $\Delta \log \text{SFR}$, for TNG and SIMBA, from left to right, respectively. The coloured background is the probability density distribution, as described in Figure 2. The solid red line is plotted by median values with errors estimated from the 16th–84th percentile ranges, and is simply distinguished by high and low spin.

momentum. In TNG, the decline in $\Delta \log \text{SFR}$ with decreasing f_{cold} reflects the trend seen in SIMBA. For quenched galaxies, the association between $\Delta \log \text{SFR}$ and f_{cold} is considerably weaker because the cold gas in CGM is not actively involved in star formation. However, there are very few quenched galaxies with $\lambda_{\text{CGM}} < 0.5$, which is in stark contrast to the results in SIMBA. The physical mechanisms behind these differences will be examined in Sect. 3.4.

3.3. Environmental effect

According to classical galaxy formation theory, galaxies gain angular momentum by accreting gas from their host halos as they evolve, influenced by the torque field (Peebles 1969; Mo et al. 1998), consistent with findings in Lu et al. (2022). Figure 6 illustrates the relationship between the angular momentum of the CGM (j_{CGM}) and that of the environment (j_{Env}) within the range of $2R_{\text{hsm}} - 100$ kpc for galaxies of $\log(M_*/M_{\odot}) > 9.5$. The top and bottom panels reveal the results for SIMBA and TNG simulations, respectively, distinguishing star-forming galaxies (SFGs, shown by blue points) from quenched galaxies (QGs, depicted by orange circles). The median values of j_{CGM} for the two populations in different j_{Env} bins are shown with solid lines. It is apparent that the CGM angular momentum, j_{CGM} , is

influenced by the environmental angular momentum, j_{Env} , for both SFGs and QGs in both simulations. This indicates that the galaxy’s angular momentum is largely inherited from its surrounding environment. But the correlation between j_{CGM} and j_{Env} decreases at lower values of j_{Env} .

Interestingly, the SFGs in two different simulations demonstrate a similar relationship between j_{CGM} and j_{Env} . The angular momentum of the CGM is influenced by both the inner stellar disc and the outer halo environment. When j_{Env} is large, the environment primarily contributes to j_{CGM} . Consequently, the SFGs and QGs in both simulations converge for $\log(j_{\text{Env}}/\text{kpc km s}^{-1}) > 3.5$, with a slope of $j_{\text{CGM}}/j_{\text{Env}}$ near unity. Conversely, at low j_{Env} values, the inner disc’s influence becomes significant, making the $j_{\text{CGM}}/j_{\text{Env}}$ slope approach zero. This accounts for the behaviour of the SFGs in the simulations, which are likely to be significantly influenced by powerful AGN feedback. We note that j_{CGM} and j_{Env} cover the same range of CGM ($2R_{\text{hsm}} - 100$ kpc) and, in principle, are closely connected. It would be intriguing to compare the relation between j_{CGM} and j_{gal} , where j_{gal} is the angular momentum calculated using all particles within $2R_{\text{hsm}}$ of each galaxy. We find that j_{Env} and j_{gal} are closely correlated with each other, and the relations between j_{CGM} and j_{gal} still largely follow the trends between j_{CGM} and j_{Env} .

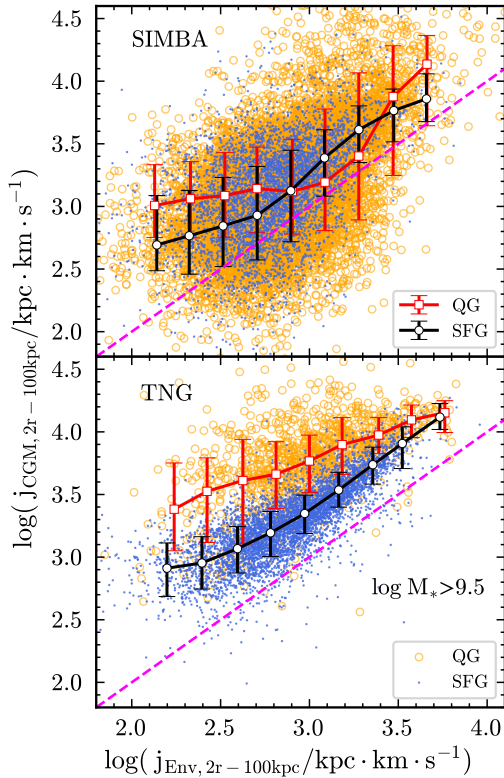


Fig. 6. Relations between j_{CGM} and j_{Env} within $2R_{\text{hsm}}$ to 100kpc , for SIMBA and TNG, from top to bottom, respectively. The black line is the relation of SFGs and red line is the relation of QGs in each panel. To show the trend more clearly, we present 1:1 baselines, indicated by the magenta dotted lines. For SFGs and QGs, each sample is plotted with a blue dot and an orange circle, respectively. Each line shows the median values, with errors estimated from the 16th–84th percentile ranges.

The primary difference between the two simulations is that QGs in the TNG simulation consistently exhibit higher j_{CGM} compared to their star-forming counterparts at a specific j_{Env} , a trend also observed in Lu et al. (2022). However, the median values of j_{CGM} for QGs in the SIMBA simulation are roughly the same as those of SFGs. The distribution of j_{CGM} for QGs is significantly broader. This distinct behaviour of QGs in the two simulations is most likely caused by the predominant impact of the AGN feedback mechanisms.

3.4. Effect of AGN feedback

The SIMBA simulation set comprises three variations of the implementation of the AGN feedback model by disabling different AGN feedback modes, as described in Sect. 2.2. To examine the influence of AGN feedback on the CGM angular momentum, we compare the fiducial model with the different variations. Figure 7 illustrates the relationship between j_{CGM} and j_{Env} for these model variations. The models displayed from left to right are the fiducial model, ‘No-Xray’, ‘No-jet’, and ‘No-AGN’ runs. These simulations use a smaller volume of $50^3 h^{-3}\text{Mpc}^3$, resulting in fewer galaxies compared to the fiducial run in Figure 6. We show the median values of j_{CGM} in different j_{Env} bins for SFGs and QGs as the black and red dashed lines, respectively. For fair comparisons, we also replicate in each panel the median values of j_{CGM} from SIMBA100 in Figure 6 as solid lines. The median j_{CGM} for SFGs in the SIMBA50 variation models closely follows

the fiducial one in SIMBA100, as expected. But there are slightly larger differences for QGs. The scatters of j_{CGM} in QGs are significantly increased when more AGN feedback mechanisms are included, confirming the results shown in Figure 6.

AGN feedback serves as the principal mechanism to quench galaxies in SIMBA. The ‘No-AGN’ run, which disables all AGN feedback modes, shows only a small number of QGs. It is clear that the j_{CGM} distribution for QGs matches that of SFGs when jet-mode feedback is disabled in both the ‘No-jet’ and ‘No-AGN’ runs. Kinetic jet feedback leads to a notable increase in the scatter of j_{CGM} for QGs. As outlined in Davé et al. (2019) (and further discussed in Ma et al. 2022), the bipolar kinetic feedback in the low-accretion mode ejects gas particles from within the black hole accretion kernel at an outflow velocity of up to 8000 km s^{-1} . The collimated nature of the outflow restricts its extent to approximately 1 kpc . As a result, the cold gas distribution in the centres of the galaxies is not severely affected by the jet-mode feedback, as also shown in Fig. 5 of Ma et al. (2022). However, jet energy is effectively distributed spherically within the CGM gas due to hydrodynamic interactions between the outflow and the CGM gas, thus modifying the distribution j_{CGM} and significantly reducing the cold gas content in the CGM.

TNG has significantly different AGN feedback mechanisms. During its low-accretion kinetic feedback phase, gas cells around a black hole are expelled with momentum in random directions. However, the mean momentum is preserved over numerous energy injection events. Despite the isotropic nature of kinetic energy release in TNG, bipolar gas outflows are still present. As discussed in Nelson et al. (2019a), the collimated outflow in TNG is largely caused by a ‘path of least resistance’ effect. Kinetic feedback-driven outflows encounter enhanced resistance on the planes of galactic discs and are reshaped into high-velocity collimated outflows perpendicular to the discs. Meanwhile, outflows along the plane of a disc will expel gas from the centre of the galaxy, which explains the void observed in the CGM gas distribution in Figure 4, as well as the extensive cold gas disc in the QG.

The influence of kinetic feedback on the CGM gas distribution depends on both the feedback mechanism and the strength of the released energy. Due to the mild energy release, the outflow velocity in TNG can only reach a maximum value around 3000 km s^{-1} in very massive galaxies (Nelson et al. 2019a), which is significantly smaller than the typical outflow velocity (with a maximum value of 8000 km s^{-1}) in SIMBA (Davé et al. 2019). As reported in Ma et al. (2022), kinetic AGN feedback causes the cold gas in TNG to migrate from the inner discs to the outer regions while maintaining the overall cold gas mass. When the cold gas is redistributed in the outer region, due to momentum conservation, the angular momentum of the CGM will increase accordingly, as shown in the right panel of Figure 6.

To gain a deeper understanding of how CGM angular momentum and AGN feedback influence the gas distribution, Figure 8 displays the galaxy distributions within the $\log f_{\text{cold}} - \Delta \log \text{SFR}$ plane for the various AGN feedback models of SIMBA50. The distributions for galaxies with $\lambda_{\text{CGM}} \geq 0.5$ and $\lambda_{\text{CGM}} < 0.5$ are illustrated in the top and bottom panels, respectively. We used the same galaxy mass range and colour scales as in Figure 5. The dashed magenta line in each panel represents the median values of f_{cold} in different $\Delta \log \text{SFR}$ bins.

When comparing the upper and lower panels within identical AGN feedback models, it is evident that the CGM angular momentum does not notably influence the relationship between the gas reservoir and the SFR in SIMBA, in agreement with the result depicted in Figure 5. There is a subtle trend indicating

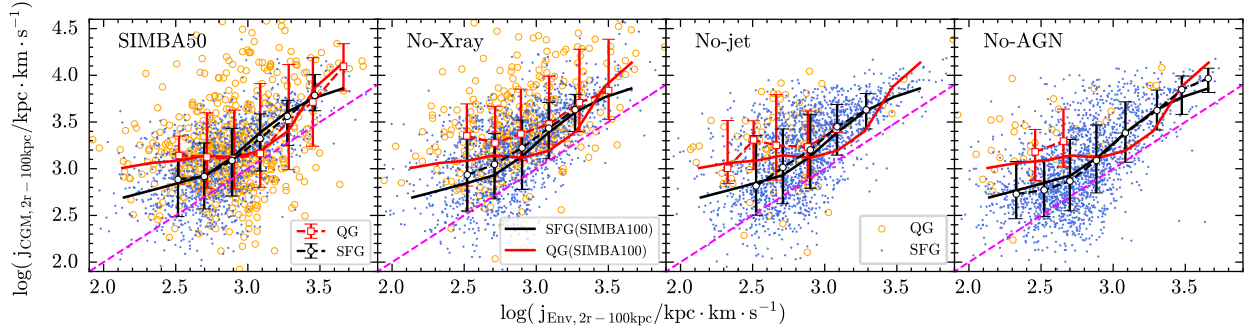


Fig. 7. Same as Fig. 6, but for the fiducial SIMBA50 run, No-Xray run, No-jet run, and No-AGN run, respectively. The black and red dashed lines show the relations of SFGs and QGs in SIMBA50, respectively. To clearly illustrate the effect of feedback, we replicate in each panel the medians for SFGs and QGs in SIMBA100 with black and red solid lines, respectively.

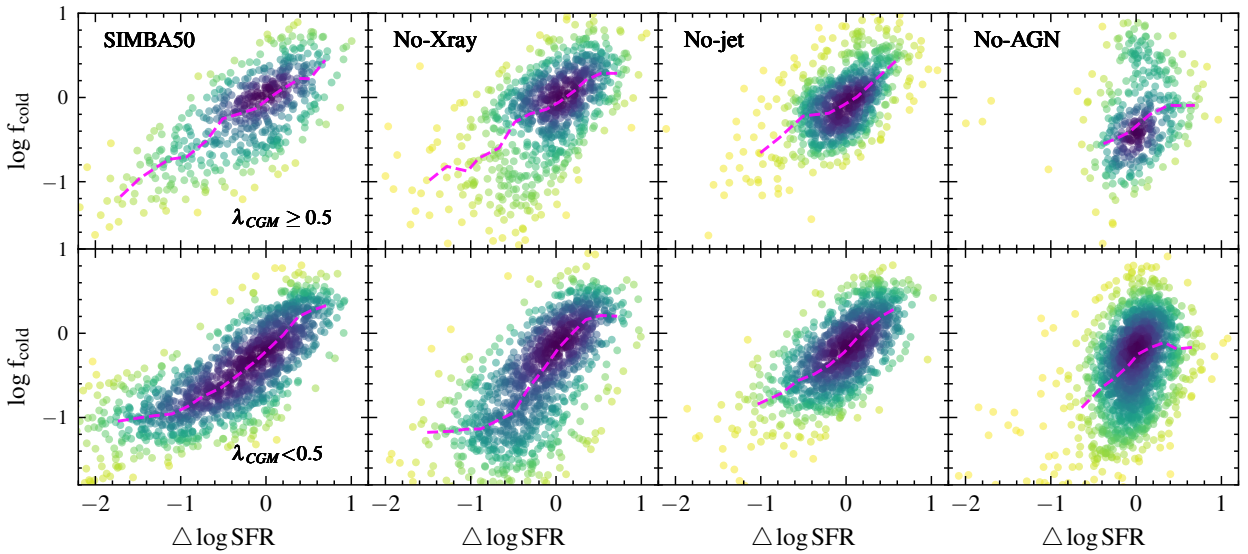


Fig. 8. Relations between $\Delta \log \text{SFR}$ and f_{cold} , for central galaxies with $\lambda_{\text{CGM}} < 0.5$ and $\lambda_{\text{CGM}} \geq 0.5$ in SIMBA50. Here we show relations of fiducial SIMBA50 run, No-Xray run, No-jet run, and No-AGN run, from left to right, respectively. The background is a probability density distribution of central galaxies, as described in Figure 2. Magenta lines show the change of medians of f_{cold} with the change of $\Delta \log \text{SFR}$.

that QGs with higher spins have a slightly stronger dependency of f_{cold} on $\Delta \log \text{SFR}$. However, due to the significant scatter, the results for low and high spins are consistent with each other, similarly shown in Figure 5, and this holds even when AGN feedback is disabled.

In summary, the AGN feedback mechanisms will considerably influence the distribution of the CGM angular momentum, as well as the cold gas in the CGM (as illustrated in Figure 4). Nonetheless, the correlation between f_{cold} and $\Delta \log \text{SFR}$ is not strongly altered by AGN feedback or CGM angular momentum.

4. Conclusions and discussions

In this research, we explore the impact of CGM angular momentum on star formation processes within galaxies. Employing advanced hydrodynamical simulations from TNG and SIMBA, we have quantified the effects of CGM angular momentum across various AGN feedback scenarios. The key findings of our study are summarised as follows.

(i) The distributions of galaxies in the $\lambda_{\text{CGM}}-\Delta \log \text{SFR}$ plane differ significantly between TNG and SIMBA. The most noteworthy distinction between these simulations is that most QGs in TNG exhibit high CGM angular momentum, whereas in SIMBA

the opposite is observed. Both simulations show similar distributions of λ_{CGM} for SFGs. Additionally, in TNG, QGs generally possess a large cold gas disc in the CGM, and the central cavity in the gas distribution is due to kinetic AGN feedback. However, QGs in SIMBA have minimal cold gas in the CGM and typically lack prominent cold gas discs, in line with their low CGM spin.

(ii) The angular momentum of the CGM is influenced by both the angular momentum of the environment and the feedback from inner stellar discs (notably the AGN feedback). The SFGs in both TNG and SIMBA exhibit similar strong correlations between j_{CGM} and j_{Env} , with a slope near unity for high j_{Env} values. At lower j_{Env} , j_{CGM} is more impacted by inner stellar discs and shows a weaker dependence on j_{Env} . On the other hand, TNG and SIMBA's QGs show markedly different distributions in the $j_{\text{CGM}}-j_{\text{Env}}$ space. In TNG, QGs have consistently higher j_{CGM} than SFGs with the same j_{Env} , resulting from randomised momentum injection events in the kinetic AGN feedback mode. Meanwhile, QGs in SIMBA have median j_{CGM} values similar to SFGs, but the scatter is significantly larger due to collimated jet-mode feedback.

(iii) While the AGN feedback and CGM angular momentum affect the cold gas distribution within the CGM, the relationship between f_{cold} and $\Delta \log \text{SFR}$ remains largely consistent across

various AGN feedback models in SIMBA50. This indicates that the star formation process steadily relies on the availability of cold gas in the CGM.

Angular momentum quenching has previously been suggested as another mechanism to quench galaxies (Peng & Renzini 2020). According to Lu et al. (2022), the high angular momentum of CGM in the QGs of the TNG might be instrumental in preserving their quenched state. Our findings indicate that the CGM angular momentum distribution in SFGs and QGs is heavily influenced by the AGN feedback mechanisms implemented in various simulations. In SIMBA, the jet-mode AGN feedback primarily depletes the cold gas in the CGM of QGs, resulting in these QGs typically having low CGM spins. This indicates that a high CGM angular momentum is not always essential for QGs. Finally, in Appendix A, we show that our results are not affected by the simulation resolutions.

Observationally, galaxies that possess relatively large HI discs (i.e. HI-rich) in comparison to typical galaxies with identical stellar masses have also been found (see e.g., Lemonias et al. 2014; Lutz et al. 2018). These galaxies exhibit high CGM angular momenta that contribute to the stabilisation of cold-gas discs and the reduction in star formation efficiency (Obreschcow et al. 2016; Lutz et al. 2018). However, these galaxies remain predominantly SFGs, with high CGM angular momentum supporting the large HI discs, unlike the QGs in TNG.

The red spiral galaxies appear analogous to the QGs in TNG in reality, characterised by their red central regions and higher HI gas fractions when compared to elliptical galaxies of comparable mass (Hao et al. 2019; Guo et al. 2020; Zhou et al. 2021). Nevertheless, as shown in Wang et al. (2022a), these red spiral galaxies with higher HI masses often exhibit bluer outer discs, suggesting that optically selected red spirals are not completely quenched. Using the HI observations from ALFALFA (Haynes et al. 2018), Guo et al. (2021) demonstrated that the optical morphology of a galaxy does not influence the relationship between total HI mass and SFR. Therefore, the primary characteristic of the cold gas discs in the CGM of QGs in TNG is largely due to its unique AGN feedback mechanism (Guo et al. 2022; Ma et al. 2022). Future studies of CGM gas and more sophisticated simulation models will offer a deeper understanding of the impact of CGM angular momentum on star formation activities.

Acknowledgements. We thank the reviewer for the constructive report that significantly improves the presentation of this paper. This work is supported by the National SKA Program of China (grant No. 2020SKA0110100), the CAS Project for Young Scientists in Basic Research (No. YSBR-092), the National Natural Science Foundation of China (No. 12433003), and the science research grants from the China Manned Space Project with NOs. CMS-CSST-2021-A02. W.C. is supported by the STFC AGP Grant ST/V000594/1, the Atracción de Talento Contract no. 2020-T1/TIC-19882 was granted by the Comunidad de Madrid in Spain, and the science research grants were from the China Manned Space Project. W.C. thanks the Ministerio de Ciencia e Innovación (Spain) for financial

support under Project grant PID2021-122603NB-C21 and HORIZON EUROPE Marie Skłodowska-Curie Actions for supporting the LACEGAL-III project with grant number 101086388. We acknowledge the use of the High Performance Computing Resource in the Core Facility for Advanced Research Computing at the Shanghai Astronomical Observatory.

References

- Anglés-Alcázar, D., Özel, F., Davé, R., et al. 2015, *ApJ*, **800**, 127
 Anglés-Alcázar, D., Davé, R., Faucher-Giguère, C.-A., Özel, F., & Hopkins, P. F. 2017, *MNRAS*, **464**, 2840
 Appleby, S., Davé, R., Sorini, D., Storey-Fisher, K., & Smith, B. 2021, *MNRAS*, **507**, 2383
 Bacon, R., Copin, Y., Monnet, G., et al. 2001, *MNRAS*, **326**, 23
 Barnes, J., & Efstathiou, G. 1987, *ApJ*, **319**, 575
 Bondi, H. 1952, *Liege International Astrophysical Colloquia*, **4**, 332
 Bullock, J. S., Dekel, A., Kolatt, T. S., et al. 2001, *ApJ*, **555**, 240
 Cappellari, M., Emsellem, E., Bacon, R., et al. 2007, *MNRAS*, **379**, 418
 Davé, R., Anglés-Alcázar, D., Narayanan, D., et al. 2019, *MNRAS*, **486**, 2827
 Driver, S. P., Allen, P. D., Liske, J., & Graham, A. W. 2007, *ApJ*, **657**, L85
 Emsellem, E., Cappellari, M., Krajnović, D., et al. 2007, *MNRAS*, **379**, 401
 Fall, S. M. 1983, in *Internal Kinematics and Dynamics of Galaxies*, ed. E. Athanassoula, 100, 391
 Fall, S. M., & Efstathiou, G. 1980, *MNRAS*, **193**, 189
 Fall, S. M., & Romanowsky, A. J. 2013, *ApJ*, **769**, L26
 Guo, R., Hao, C.-N., Xia, X., et al. 2020, *ApJ*, **897**, 162
 Guo, H., Jones, M. G., Wang, J., & Lin, L. 2021, *ApJ*, **918**, 53
 Guo, H., Jones, M. G., & Wang, J. 2022, *ApJ*, **933**, L12
 Hao, C.-N., Shi, Y., Chen, Y., et al. 2019, *ApJ*, **883**, L36
 Haynes, M. P., Giovanelli, R., Kent, B. R., et al. 2018, *ApJ*, **861**, 49
 Hopkins, P. F. 2015, *MNRAS*, **450**, 53
 Hopkins, P. F., & Quataert, E. 2011, *MNRAS*, **415**, 1027
 Kennicutt, R. C., Jr 1998, *ARA&A*, **36**, 189
 Kereš, D., Katz, N., Weinberg, D. H., & Davé, R. 2005, *MNRAS*, **363**, 2
 Krumholz, M. R., & Gnedin, N. Y. 2011, *ApJ*, **729**, 36
 Lemonias, J. J., Schiminovich, D., Catinella, B., Heckman, T. M., & Moran, S. M. 2014, *ApJ*, **790**, 27
 Lu, S., Xu, D., Wang, S., et al. 2022, *MNRAS*, **509**, 2707
 Lutz, K. A., Kilborn, V. A., Koribalski, B. S., et al. 2018, *MNRAS*, **476**, 3744
 Ma, W., Liu, K., Guo, H., et al. 2022, *ApJ*, **941**, 205
 Marinacci, F., Vogelsberger, M., Pakmor, R., et al. 2018, *MNRAS*, **480**, 5113
 Mo, H. J., Mao, S., & White, S. D. M. 1998, *MNRAS*, **295**, 319
 Naiman, J. P., Pillepich, A., Springel, V., et al. 2018, *MNRAS*, **477**, 1206
 Nelson, D., Pillepich, A., Springel, V., et al. 2018, *MNRAS*, **475**, 624
 Nelson, D., Pillepich, A., Springel, V., et al. 2019a, *MNRAS*, **490**, 3234
 Nelson, D., Springel, V., Pillepich, A., et al. 2019b, *Comput. Astrophys. Cosmol.*, **6**, 2
 Obreschcow, D., Glazebrook, K., Kilborn, V., & Lutz, K. 2016, *ApJ*, **824**, L26
 Peebles, P. J. E. 1969, *ApJ*, **155**, 393
 Peng, Y.-J., & Renzini, A. 2020, *MNRAS*, **491**, L51
 Pillepich, A., Springel, V., Nelson, D., et al. 2018, *MNRAS*, **473**, 4077
 Rahmati, A., Pawlik, A. H., Raičević, M., & Schaye, J. 2013, *MNRAS*, **430**, 2427
 Romanowsky, A. J., & Fall, S. M. 2012, *ApJS*, **203**, 17
 Schmidt, M. 1959, *ApJ*, **129**, 243
 Springel, V. 2010, *MNRAS*, **401**, 791
 Springel, V., Pakmor, R., Pillepich, A., et al. 2018, *MNRAS*, **475**, 676
 van de Sande, J., Scott, N., Bland-Hawthorn, J., et al. 2018, *Nat. Astron.*, **2**, 483
 Vogelsberger, M., Genel, S., Springel, V., et al. 2014, *MNRAS*, **444**, 1518
 Wang, L., Zheng, Z., Hao, C.-N., et al. 2022a, *MNRAS*, **516**, 2337
 Wang, S., Xu, D., Lu, S., et al. 2022b, *MNRAS*, **509**, 3148
 Weinberger, R., Springel, V., Hernquist, L., et al. 2017, *MNRAS*, **465**, 3291
 Zhou, S., Li, C., Hao, C.-N., et al. 2021, *ApJ*, **916**, 38

Appendix A: Resolution effect

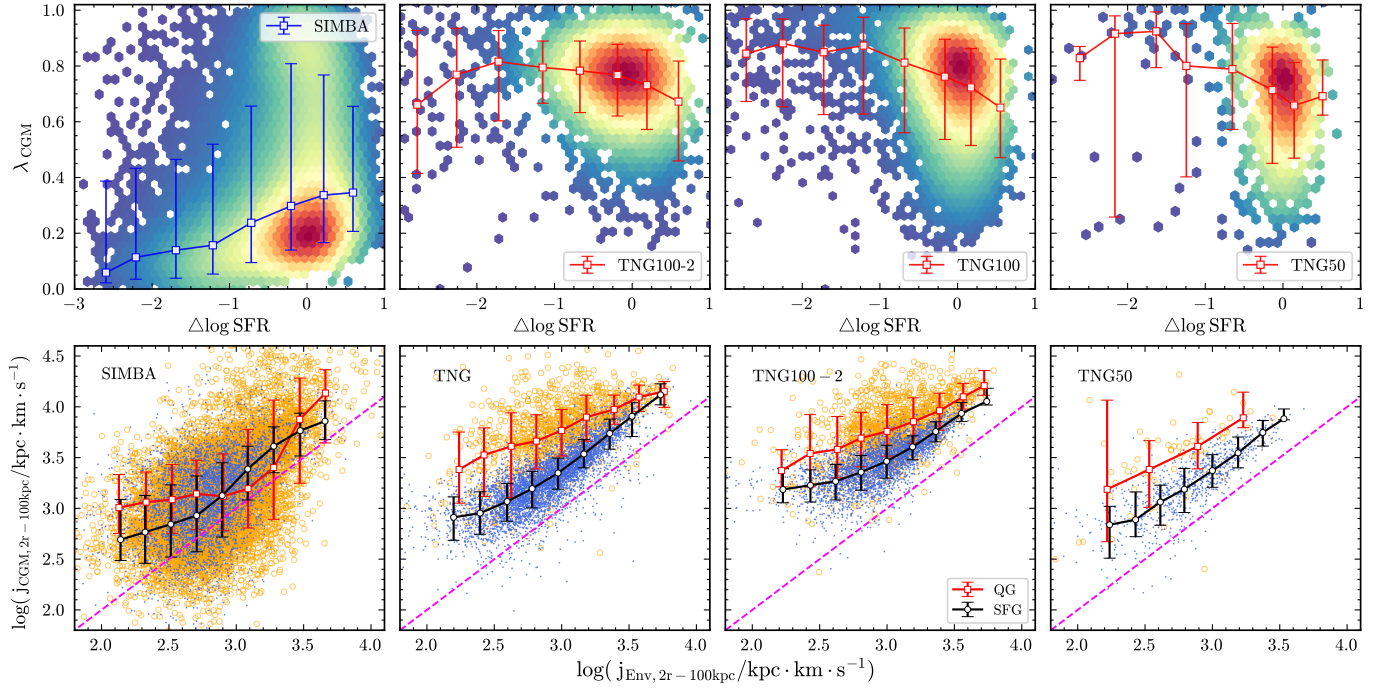


Fig. A.1. Same to Figs. 2 and 6, but also including the results for TNG100-2 and TNG50. Overall, the trends in TNG100-2 and TNG50 are very similar to that in TNG100, with weak dependence on resolution. The quenched galaxies in TNG100-2 and TNG50 still show a higher λ_{CGM} than their star-forming counterparts.

In order to check whether our main results will be affected by the resolutions of the specific TNG and SIMBA simulations used in this paper, we investigate the two primary results in TNG100-2 and TNG50. We show the distribution of λ_{CGM} as a function of $\Delta \log \text{SFR}$ and the relations between j_{CGM} and j_{Env} , as illustrated in Figure A.1. We repeat the results of TNG100 and SIMBA for better comparisons. TNG100-2 has the same box size as TNG100, with mass resolutions lower than TNG100, but very similar to those of SIMBA. The dark matter mass resolution is $m_{\text{DM}} = 6.0 \times 10^7 M_{\odot}$, and the average gas mass is around $1.1 \times 10^7 M_{\odot}$ in TNG100-2. TNG50 simulation has a box size of $35 h^{-1} \text{Mpc}$ on a side, with a dark matter mass resolution of $m_{\text{DM}} = 4.5 \times 10^5 M_{\odot}$ and an average gas mass around $8.5 \times 10^4 M_{\odot}$, which are significantly higher than those of TNG100 and TNG100-2. Here, we confirm that, even though the exact values of λ_{CGM} and j_{CGM} will be affected by the simulation resolution, our results remain unchanged in simulations of different resolutions.